UC San Diego
UC San Diego Previously Published Works

Title

The shape of Nature's stingers revealed

Permalink

Journal

ISSN

Authors

Quan, Haocheng
Liang, Xudong
Zhang, Xuan
et al.

Publication Date

DOI

Peer reviewed

The shape of Nature's stingers revealed

Haocheng Quan[a,b,1] (ID), Xudong Liang[c] (ID), Xuan Zhang[d], Marc A. Meyers[e], Robert M. McMeeking[b,f], and Eduard Arzt[b,g,h,1] (ID)

Stinger-like structures in living organisms evolved convergently across taxa for both defensive and offensive purposes, with the main goal being penetration and damage. Our observations over a broad range of taxa and sizes, from microscopic radiolarians to narwhals, reveal a self-similar geometry of the stinger extremity: the diameter (d) increases along the distance from the tip (x) following a power law $x \sim d^n$, with the tapering exponent varying universally between 2 and 3. We demonstrate, through analytical and experimental mechanics involving three-dimensional (3D) printing, that this geometry optimizes the stinger's performance; it represents a trade-off between the propensity to buckle, for n smaller than 2, and increased penetration force, for n greater than 3. Moreover, we find that this optimal tapering exponent does not depend on stinger size and aspect ratio (base diameter over length). We conclude that for Nature's stingers, composed of biological materials with moduli ranging from hundreds of megapascals to ten gigapascals, the necessity for a power-law contour increases with sharpness to ensure sufficient stability for penetration of skin-like tissues. Our results offer a solution to the puzzle underlying this universal geometric trait of biological stingers and may provide a new strategy to design needle-like structures for engineering or medical applications.

bioinspiration | buckling | penetration | biomechanics

Stingers usually refer to the sharp pointed out-thrusts on living organisms, and their bynames include spines, spikes, thorns, needles, quills, and tusks. They are one of the most ubiquitous structural elements and result from convergent evolution across taxa, ranging from unicellular organisms to large mammals such as narwhal whales. Despite their length spanning over six orders of magnitude and the composition varying from pure minerals to collagen-hydroxyapatite composites, the morphology of biological stingers shares a similar geometric trait: a tapered slender cylindrical column with a sharp tip (Fig. 1*A*).

Serving primarily as an invasive weapon, the design principle of stingers requires structural stability to avoid buckling or fracture; on the other hand, they must be sufficiently sharp to penetrate tissue without excessive force. Previous studies on the structural optimization of biological stingers mostly focused on their hierarchical microstructures or materials heterogeneity (3–6) and the investigations usually concentrated on individual cases. Only a few attempts were made to unfold the universal design strategy of diverse biological stingers, despite the striking resemblance of their global contours. McMahon, Bonner, and Bonner (7) pioneered the investigation of the scaling law of synthetic nails and spikes and predicted that to maintain mechanical stability when scaling up these structures, their base diameter and length, noted as d_0 and L, respectively, should follow an allometric relationship of $d_0 \sim L^{2/3}$. However, their analysis is based on a straight cylinder model, without capturing the nature of tapering for a typical stinger-like structure. Jensen et al. (8) investigated the optimal design principle of biological stingers across species using a tapered cylindrical model; They revealed that the length L and base diameter d_0 actually follow an isometric relationship $d_0 \approx \alpha L$, where α is a constant determined by the elastic modulus of the stinger material and the friction force during the penetration process. They assumed the column to be tapered linearly and concluded that the geometry is optimized in the trade-off between maximizing the buckling resistance, which requires a larger d_0/L, and minimizing the penetration barrier, which demands a lower ratio. Regarding the concepts for tapering that are other than linear, Freeman and Leman (9) proposed the optimal shape of canine teeth to be a paraboloid-like cone to balance structural strength and penetration ability. Such a power-law taper was recently confirmed by Evans et al. (10) among diverse sharp-pointed structures in Nature. However, no mechanical insight was provided to explain such a structural design.

Here, we investigate the shape of the stinger extremity in ten different organisms, including radiolarians, bees, cacti, and narwhal whales and find that it departs from linearity in a universal way. Through a combination of analytical and experimental mechanics involving 3D printing of prototype shapes, our assessment identifies an optimized

Significance

As ubiquitous defense mechanisms in Nature, stinger-like structures cover a size range over six orders of magnitude. While their composition varies, we uncovered a common geometric trait: a non-linear relationship between diameter and distance from the tip, following a power law with an exponent universally between 2 and 3. Through a combination of theoretical mechanics and experiments, we interpret this universal shape to be the result of a competition between penetration and buckling, motivated by the limitations of the mechanical properties of the stinger material. Our study not only resolves a mystery underlying the structural optimization of convergently evolved natural stingers, but also can offer inspiration for efficient needles in technology or biomedicine, made from sustainable non-metallic materials.

penetration ability which has, presumably, enhanced survival across species.

Results

Power-Law Taper of the Stinger Shape. Biological stingers from five representative organisms are presented in Fig. 1*A*. Despite their lengths ranging from tens of micrometers to meters and their compositions varying across silica, chitin, cellulose, keratin, and mineralized collagen, their profiles—especially the segment close to the tip—are strikingly similar. To quantify this geometric trait, the diameter d at various distances, x, from the tip is measured (*Inset* of Fig. 1*B*). Results for ten biological stingers are shown in the log–log diagram in Fig. 1*B*; the data for each stinger are well aligned linearly (fine dashed lines), indicating a power-law relationship between d and x. For linear fitting and slopes, see also *SI Appendix*, Figs. S1

and S2 and Table S1. These measurements demonstrate that the stalks of stingers near the tip are not conical but have a defined shape deviating significantly from linearity and obeying a power law relationship, $x \sim d^n$. Regardless of size and composition, n is approximately around 2 to 3. This is consistent with results in the literature (9, 10), where measurements of canine teeth (9) resulted in $n \approx 1.8$. Stinger profiles with taper exponents from 1 to 5 are sketched in Fig. 1*C*, where d and x are normalized by the base diameter d_0 and the total stinger length L_0, respectively. Note that in Fig. 1*C*, the profile is truncated at its tip, leading to a finite diameter there, as in most biological examples; we will return to this approximation below. In comparison with linear tapering ($n = 1$), the power-law taper, with $n > 1$, widens the cross-section of stingers nonuniformly along the longitudinal axis. The case of a taper with $n = 2$ is shown by the thicker red line in Fig. 1*C*, and our results for natural stingers are located in the hatched region ($2 \le n \le 3$).
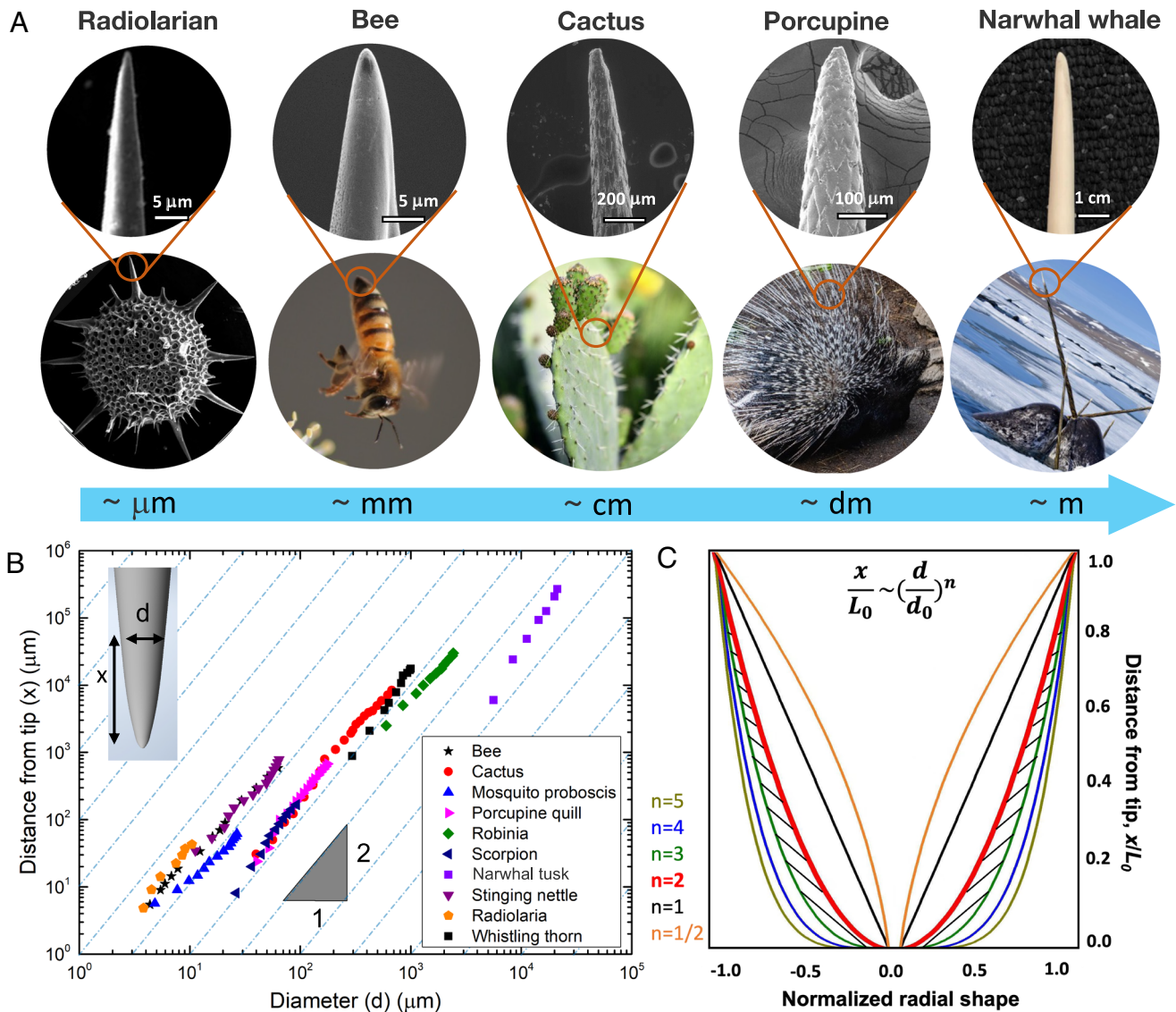
Fig. 1. The geometry of biological stinger tips. (*A*) Stingers from selected organisms across taxa; from *Left* to *Right*: radiolarian (silica), bee (chitin), cactus (cellulose), porcupine (keratin), and narwhal whale (mineralized collagen). Their sizes span six orders of magnitude. (*B*) Variation of diameter along the longitudinal axis, as illustrated in the *Inset*, measured for 10 biological stingers and plotted in logscale. The blue dash lines indicate the slope of 2. (*C*) Schematic profile of power-law tapered stingers with exponents of 1/2, 1, 2, 3, 4, and 5. The shapes of most biological stingers are found within the hatched region, between contours for $n = 2$ (thick red line) and $n = 3$. The profile is truncated at the tip, leading to a finite diameter there. (Source of images: Radiolarian and stinger tip adapted from ref. 1; bee, cactus, and porcupine from www.unsplash.com; tip of porcupine quill adapted from ref. 2; narwhal whale from Paul Nicklen Photography and tusk tip adapted from www.inuitsculptures.com. Details on the measurements for *B* are provided in *Methods*.)

Model Experiments and Analysis. We hypothesize that a competition between buckling and penetration determines the geometry, and that the intersection of the buckling load and the penetration force determines the ideal shape. Experiments using 3D-printed stingers, with pinned–pinned boundary conditions (BCs), establish the buckling loads and soft polymer substrates are used to determine the penetration threshold. The material of the synthetic stingers is Splint 385 (Dentona, Dortmund, Germany), a metacrylate-based dental resin with an elastic modulus in the cured state of the same order of magnitude as for natural stingers (11). The soft substrate is fabricated from PDMS (polydimethylsiloxane) (Sylgard 184), with a Young's modulus of approximately 1 MPa; PDMS has been widely used as an artificial mechanical skin model in the evaluation of transdermal medical devices (12). Details of our experimental setup are elaborated in the *Methods* section.

For both experimentation and numerical analysis, the stinger tip shape was truncated at a diameter of 0.5 mm. The resulting tip shapes are consistent with the natural profiles illustrated in Fig. 1*C*. We note that perfectly sharp stingers are not observed in Nature and are impossible to fabricate. From a mechanical point of view, a perfectly pointed shape would buckle under a negligible applied compressive load. Blunting the tip by truncation is an approximation that avoids such easy buckling. For blunter profiles with $n > 3$, the truncation is less noticeable as it makes less difference to the overall shape (Fig. 1*C*). For 3D printing of prototype stingers, truncation was chosen in the form of a finite radius of curvature equal to 0.25 mm at the stinger tip (*Methods* section); all artificial stingers used in the experiments had this truncated tip with this finite radius of curvature.

During penetration into a soft substrate, the initial contact areas for different stinger profiles will be nearly similar, especially for relatively sharp stingers. From this, it can be deduced that, after some elastic and possibly some inelastic deformation, all of the synthetic stingers tested in the experiments will begin to penetrate the substrate at roughly the same applied force. Thereafter, the process of penetration or non-penetration will depend on the stingers' profiles.

Buckling. Successful penetration requires avoidance of buckling until the stinger can puncture the tissue, as is illustrated in Fig. 2*A*. To quantify the effect of a power-law taper on buckling resistance, a straight column with a varying circular cross section is modeled, as shown in Fig. 2*B*. With the *x*-axis originating from the center of the truncated tip, the variation of diameter $d(x)$ of a power-law profile is given by

$$\left[\frac{d(x)}{d_a}\right]^n - 1 = \frac{qx}{L_0}, \qquad \text{[1]}$$

where d_a, d_0 are the diameters of tip and base, respectively; L_0 is the total length of the stinger. The parameter q, given by $q = (d_0/d_a)^n - 1$, generates a truncated tip with a finite diameter. Note that a larger n value describes a stinger with a blunter tip.

For a given n, the critical buckling load, F_c, for pinned–pinned BCs (restricted lateral movement at two ends) is obtained from Euler buckling theory (details in the *SI Appendix*) (13). The resulting prediction of F_c as a function of n is plotted as a blue line in Fig. 2*C* for an aspect ratio $(d_0/L_0) = 0.10$, modulus $E = 1.9$ GPa, $d_0 = 4$ mm, $L_0 = 40$ mm and $d_a = 0.5$ mm. As expected, the buckling load increases with n. Experimental validation is performed on 3D-printed stingers with the same geometric profile, dimensions, and elastic modulus as in the modeling. The truncation with a hemispherical shape is expected to have little influence on the

buckling load. As can be seen in Fig. 2*C*, the experimental buckling load (squares in Fig. 2*C*) follows the same trend with increasing n as that of the theoretical model (solid blue line in Fig. 2*C*), but with a deviation from the theoretical results caused by the setup (*Inset* in Fig. 2*C*). The experimental setup imposes constraints on the rotation of column ends so that true pinned–pinned BCs are not achieved. Inspired by the "effective length" often utilized in Euler buckling theory, the same concept is adapted to model the stinger buckling behavior in our experiments. The green curve in Fig. 2*C* shows the theoretical buckling load for tapered columns with length $L_0 = 30$ mm under pinned–pinned BCs, which fits well with our experimental results. Hence, we use an effective length, $L_0^{eff} = 30$ mm, to model the buckling behavior of the synthetic stingers tested in our experiments. More experimental validation of such an effective length concept is provided in *SI Appendix*, Fig. S3, and detailed explanations are found in *Methods*.

Regardless of the BCs, the buckling load, F_c, in Fig. 2*C* rises monotonically, but not linearly with increase of the taper exponent n. It rises more rapidly in both cases when n is within the range between 2 and 4. This is seen more clearly by observing the change in slope (first derivative with respect to n) for the theoretical results for stingers of length 40 mm (blue dash-dot line in Fig. 2*C*), which shows that the slope reaches an apex at an exponent $n \approx 2.7$. This maximum indicates that there are diminishing returns in regard to improvements in buckling resistance when n is increased much above 2.7, the inflexion point.

Interestingly, our model also reveals that the exponent identified above for the inflexion point, n, is relatively insensitive to the stinger base diameter (d_0), aspect ratio $(AR = d_0/L_0)$, and material elastic modulus within the data range considered. It varies only slightly in terms of the tip-to-base diameter ratio $(TBR = d_a/d_0)$. In the results displayed in Fig. 2 *D–G*, the buckling load, F_c (*Middle*), and its derivative with respect to n (*Lower*), are plotted as functions of n for four cases, in which, *ceteris paribus*, only one of the four above-mentioned parameters is varied. The detailed values of the fixed and varied parameters are provided in Methods. As expected, widening the stinger base (Fig. 2*D*), increasing the aspect ratio (Fig. 2*E*), and increasing the elastic modulus (Fig. 2*F*) all cause the buckling load to increase, but the taper exponent, n, at the inflexion point hardly changes (as indicated by the vertical dotted lines). Decrease of the TBR causes a higher slope of F_c versus n at lower values of n, and the inflexion point moves slightly toward $n = 2$ (Fig. 2*G*). This suggests a larger benefit in regards to buckling suppression by raising n above unity for stingers with relatively sharp tips (smaller tip-to-base ratio).

Penetration. For biological stingers, the goal of enhancing the elastic stability is to enable successful penetration before buckling can occur. Since penetration is a complex process coupled with friction, large deformation of soft materials, and nonlinear fracture mechanics (8, 14–19), the impact of taper exponent on the penetration process is evaluated here experimentally. A series of stingers with the same geometry as used for the buckling tests were 3D printed with the same resin.

The penetration force as a function of the taper exponent n is presented in Fig. 3, in comparison to the buckling forces from Fig. 2*C*. Penetration is recorded as a sharp load drop in the force-displacement curves (shown in Fig. 4*B*) as opposed to a smoother transition typical of buckling (Fig. 4 *A* and *C*). Both the stinger with a linear taper ($n = 1$) and that with a large exponent ($n = 8$) buckle before successful penetration. To make the penetration force accessible to measurement for these values of n (open red circles in Fig. 3), the artificial stingers were
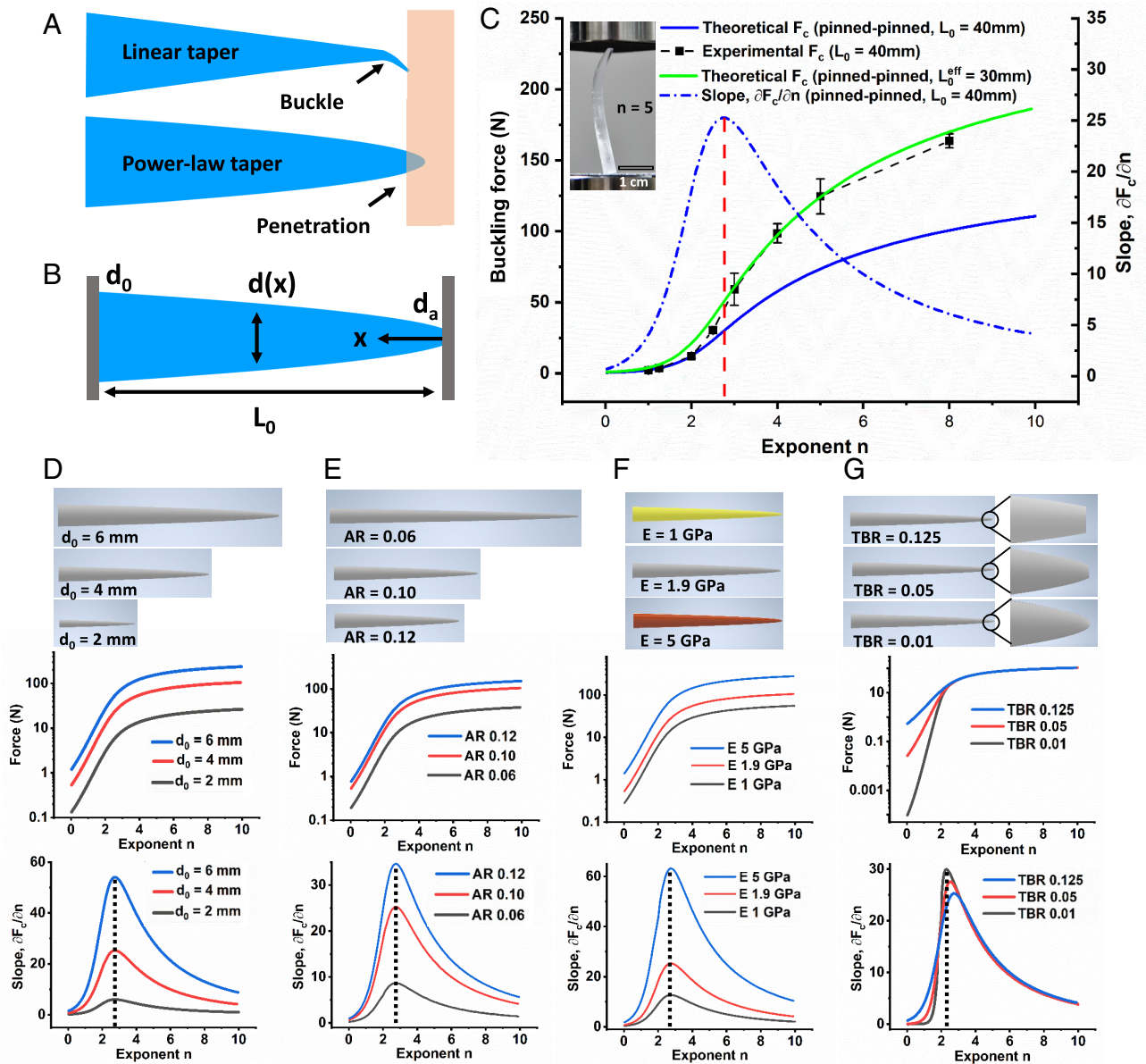
Fig. 2. Buckling of power-law tapered columns. (*A*) A linearly tapered stinger is prone to buckling, with deflection mostly confined to the tip region. The power-law taper, e.g., for $n = 2$, improves buckling resistance and ensures successful penetration. (*B*) Modeling of a tapered column. The diameter $d(x)$ varies along x; diameters of the tip and base are d_a and d_0, respectively; total stinger length is L_0. (*C*) Variation of the critical buckling load, F_c, with respect to n for pinned–pinned BCs from the experiments (shown by data points and error bars) and from theoretical calculations (shown by continuous lines). The theoretical results for $L_0 = 40$ mm are shown by the solid blue line, and its derivative with respect to n by the dash-dot blue line. The theoretical results for $L_0 = 30$ mm are shown by the solid green line. Other parameters used are $E = 1.9$ GPa, $d_0 = 4$ mm and $d_a = 0.5$ mm. The derivative of the buckling load for column length $L_0= 40$ mm peaks at $n = 2.7$. (*Inset*) image of a buckled column ($n = 5$) from the experiments. (*D–G*) Predicted buckling loads for various design parameter variations: stinger base diameter (d_0), aspect ratio ($AR = d_0/L_0$), elastic modulus (E) and tip-to-base diameter ratio ($TBR = d_a/d_0$) as shown in *D–G*, respectively. (*Top*) schematics of stinger geometries; (*Middle*) critical buckling loads for pinned–pinned BCs calculated as a function of taper exponent n; (*Bottom*) derivatives of buckling load with respect to n, all of which (*D–F*) peak at $n \sim 2.7$ (dotted line). For sharper stingers (smaller tip-to-base ratio), the peak approaches $n = 2$ (*G*). The detailed values of the parameters for *D–G* are provided in *Methods*.

redesigned to avoid buckling, but with the segment near the tip unchanged in shape (*SI Appendix*, Fig. S4). The results show that the penetration force also increases monotonically as the taper exponent n rises. We note that the penetration force lies below the critical buckling load in a "window" within which the n values range from approximately 2 to 6. Outside of this window, the penetration force exceeds the critical buckling load, and buckling will intervene. It is noteworthy that penetration is predicted to be easiest for n close to but not below 2; this is in good agreement with the power-law taper exponent observed in Nature (blue shading in Fig. 3).

To visualize the impact of the stinger taper exponent on penetration, the indent areas are imaged just before puncture after withdrawal of the stinger (Fig. 5*A*). These images indicate that permanent ("plastic") deformation is generated in the substrate before the final puncture, as evidenced by the permanent change of contrast (dark region on the images in Fig. 5*A*). Due to the varied taper exponents, the morphology and size of the plastic zones differ. For stingers with low n ($n = 1$ and 2 in Fig. 5*A*), the diameter of the plastic zone, denoted as d_p, is smaller than the diameter of the immediate stinger tip ($d_a = 0.5$ mm); in this case, the immediate tip shape will play an important role in the contact
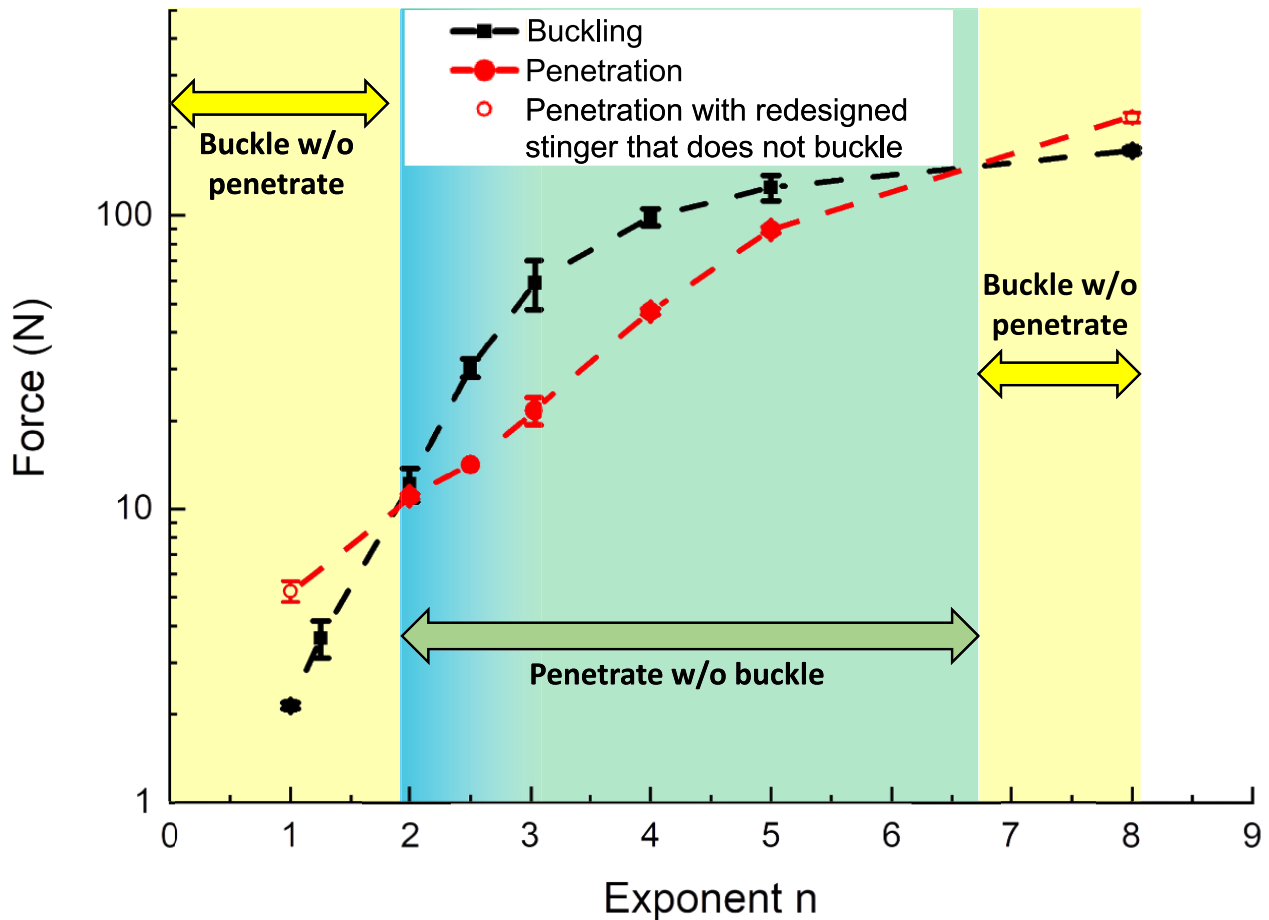
Fig. 3. Competition between penetration and buckling for synthetic stingers against PDMS. Experimentally determined variation of penetration and buckling forces for 3D-printed stingers against PDMS, as a function of *n*.

processes. In contrast, the plastic zone generated by stingers with high *n* (*n* = 5 and 8 in Fig. 5*A*) is much larger than d_a ($d_p \gg d_a$), which suggests that the final puncture is not dominated purely by the immediate tip shape. The stalk close to the tip widens significantly due to the large taper exponent (Fig. 1*C*) and this wider segment is involved in the generation of contact stress and deformation in the substrate.

Based on reports in the literature (16–19) and on our observations, the deformation of the substrate during indentation is sketched in Fig. 5*B*. Puncturing the soft substrate is caused by a combination of compression beneath the indenter and shear along the circumference of the contact edge. In our stinger models, the tip diameter (d_a) is fixed and only the taper exponent determines differences among the geometries of the stinger stalk. For stingers with low *n* (*n* ≤ 3), the stalk close to the tip widens only moderately, keeping shear stresses localized at the edge of the immediate tip end (*Left* in Fig. 5*B*), and compression concentrated in a column with diameter ~d_a. Varying of the taper exponent within the range 1 ≤ *n* ≤ 3 effectively tunes only the buckling resistance while having limited impact on the penetration threshold. For stingers with high *n* (*Right* in Fig. 5*B*), the stalk widens substantially in the region close to the tip. During indentation, the immediate contact area is much larger than the tip end (d_a), resulting in an increase in the area over which shear stresses operate and in the compressed volume of the substrate. This leads to a considerable rise in the penetration threshold, rendering a stinger with a large taper exponent less beneficial. An additional Finite Element Analysis was undertaken to chart the indentation trajectory, as

visualized in *SI Appendix*, Fig. S5. These simulations robustly validate our proposed mechanisms.

Further experiments were carried out in which stingers from Nature penetrated pigskin (*SI Appendix*, Fig. S6). The similarity of the resulting force-displacement curves to those for 3D-printed stingers penetrating into PDMS (Fig. 4*B*) provides validation for using PDMS as the penetration target in the experiments summarized in Fig. 3.

Discussion

Our comparative analysis of buckling and penetration reveals an optimized structural design for stingers: a power-law profile with a taper exponent close to 2 appears to best fulfill the conflicting requirements of easy penetration and avoidance of buckling. Such a geometry benefits from a significant rise in buckling resistance as *n* departs from 1 (linear taper in conventional models) towards 2 to 3 (paraboloid-like shape), while the force required for penetration increases less sharply. The latter phenomenon is consistent with the observation by Freeman et al. (9) in the penetration of mammal hide using a power-law tapered artificial tooth, where the penetration force changed moderately for *n* below 2.5 and increased dramatically beyond it. Our results show that the different dependences of buckling and penetration forces on the taper exponent *n* open up a window in which penetration can occur without buckling, even for comparatively compliant stinger materials. We note that the exact position of this window is rather insensitive to the parameter variations as

in Fig. 2 *D–G*, but will deviate, e.g., for modulus values far outside the 1 to 5 GPa range.

These conclusions are in good agreement with our observations from Nature, where a range between $n = 2$ and 3 is found for most biological stingers. Their mechanical optimization is the result of a co-evolution process as the outermost layer of soft organisms (the integumentary system) is usually tough and relatively stiff for protective purposes. At first sight, a very sharp, stiff stinger would seem to be an option that evolution would favor, with a tip shape that is conical, slightly tapered, and with a very small diameter tip to ease penetration. However, even when made from a stiff material, a conical tip with such characteristics will experience tip buckling at relatively low applied load (see *SI Appendix*, Eq. **S19** with $d_a \to 0$). We infer that if Nature were to develop stingers with a linear taper, they would have to be truncated at their tips with a somewhat flat end to achieve a viable critical buckling load. Therefore, in our assessment, we utilized linearly tapered stingers with a truncated blunt end. As stingers of parabolic shape also have relatively low buckling load unless truncated with a somewhat blunt tip (see *SI Appendix*, Eq. **S15** in the limit $d_a \to 0$), we chose to truncate them at their tips as well. For an objective comparison across all shapes, we were then obliged to truncate all stinger shapes at their tips with a blunt end of finite size.

Deviations from the designs discussed here are possible. For instance, the intricate stylet-lancet architecture of a bee's stinger (4) and the serrated stylet complex in mosquito proboscis (20) are more complex than what is assumed here. Yet, this complexity lessens toward the stinger's tip, maintaining the tapered column model's applicability for examining puncture events. The intricate designs, such as serrations, barbs, or paired stylets, primarily influence penetration efficacy post-puncture. Notably, many stingers, like a scorpion's, display significant curvature, diverging from our model as well. However, this curvature is typically less pronounced at the tip, where the applied force induces compression orthogonal to the substrate, facilitating target penetration (21). Thus, our experimental and analytical models capture the physics of the system structural stability and remain valid in addressing the competition between buckling and penetration. We further note that the buckling resistance of a stinger could be improved by modifying the aspect ratio to form a stalky column (Fig. 2*E*). However, this also reduces the reach distance, possibly placing the organism at a shorter distance from the predator or prey, and thereby endangering it. Such a strategy thus has its limitations.

Beyond the tapering approach we have identified, the utilization of structural and compositional gradients is yet another strategy employed by nature to construct durable stingers. These gradients can be present both in the radial and longitudinal dimensions. For instance, the external layer of many plant thorns is denser and more lignified compared to their inner core. The cuticle of a scorpion's stinger incrementally thickens from the base to the tip, culminating in a design that combines a harder tip with a more flexible base (5). Such gradual variation serves as a valuable complement to the exponent-tapering design strategy that we have outlined.

Penetration events are inherently more complex than what our experiments capture and may involve other potential failure modes for stinger tips. Tip failure, for example, can result from bending fractures when penetration occurs at an angle. Power-law tapering not only bolsters buckling resistance through its effect on the second moment of inertia but may also enhance bending resistance. Additional factors including penetration speed, along with the stinger's vibrations and rotations during penetration, are essential to the stinger's performance and its potential failure modes in various scenarios. This complexity underscores the need for further research to comprehensively understand and predict stinger effectiveness across diverse penetration contexts.

We note finally that intricate structural optimization is a necessity in Nature because of a lack of extremely hard, tough, and stiff structural materials such as metals or defect-free ceramics. Biominerals could be an option, but their intrinsic brittleness tends to preclude scale-up because of the resulting sensitivity to flaws. Instead, stingers composed of pure minerals, e.g., silica, are mostly observed in very small, unicellular organisms (22). Bulk stingers, composed of chitin, cellulose, keratin, or mineralized collagen, being materially more compliant than compositions that are predominantly mineral, must derive their robustness from a shape adaptation, as revealed in this study. In our experiments, we chose for our 3D-printed stingers a material having an elastic modulus of 1.9 GPa as that is representative of many natural stinger materials. In addition, soft PDMS is a target material that is often used as a skin model for transdermal devices. Therefore, we believe that, by utilizing reasonable material parameters, our experimental results provide insight into the reasons why natural stingers have the shapes that they do.

Extension of this work to very different materials parameters, e.g., very stiff metallic needles or extremely pliable targets, may modify some of the conclusions. Thus, our present model is confined to stingers with elastic moduli ranging from hundreds of megapascals to ten gigapascals. The substrates are modeled as soft, neo-Hookean materials with moduli ranging from several hundred kilopascals to a few megapascals, akin to the skin tissues of animals. This specificity is crucial for the optimization strategy we propose
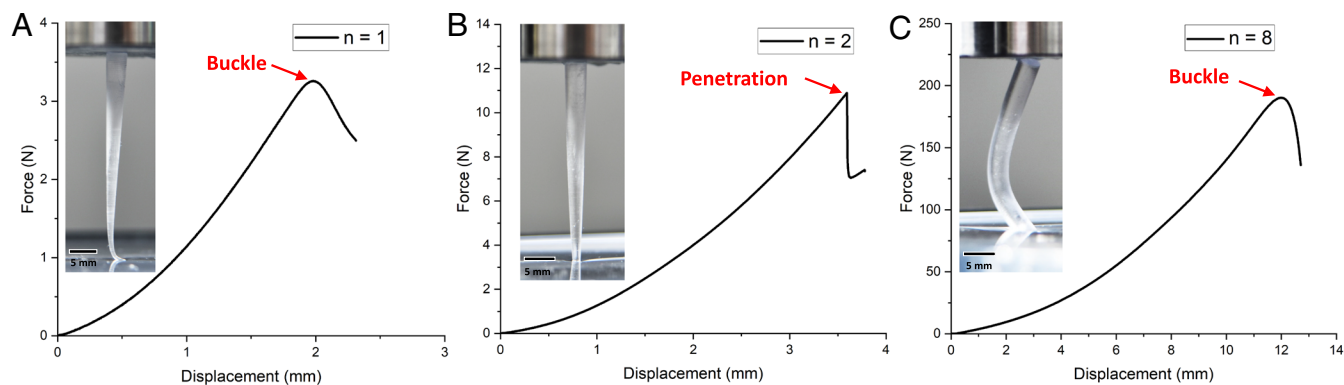
Fig. 4. Force–displacement curves for failed (*A* and *C*) and successful (*B*) penetrations of 3D-printed stingers into a PDMS substrate. (*Insets*) images showing successful penetration by the stinger with $n = 2$ (*B*) and buckling without penetration by stingers with $n = 1$ (*A*) and $n = 8$ (*C*).

A

Indent area before puncture

B
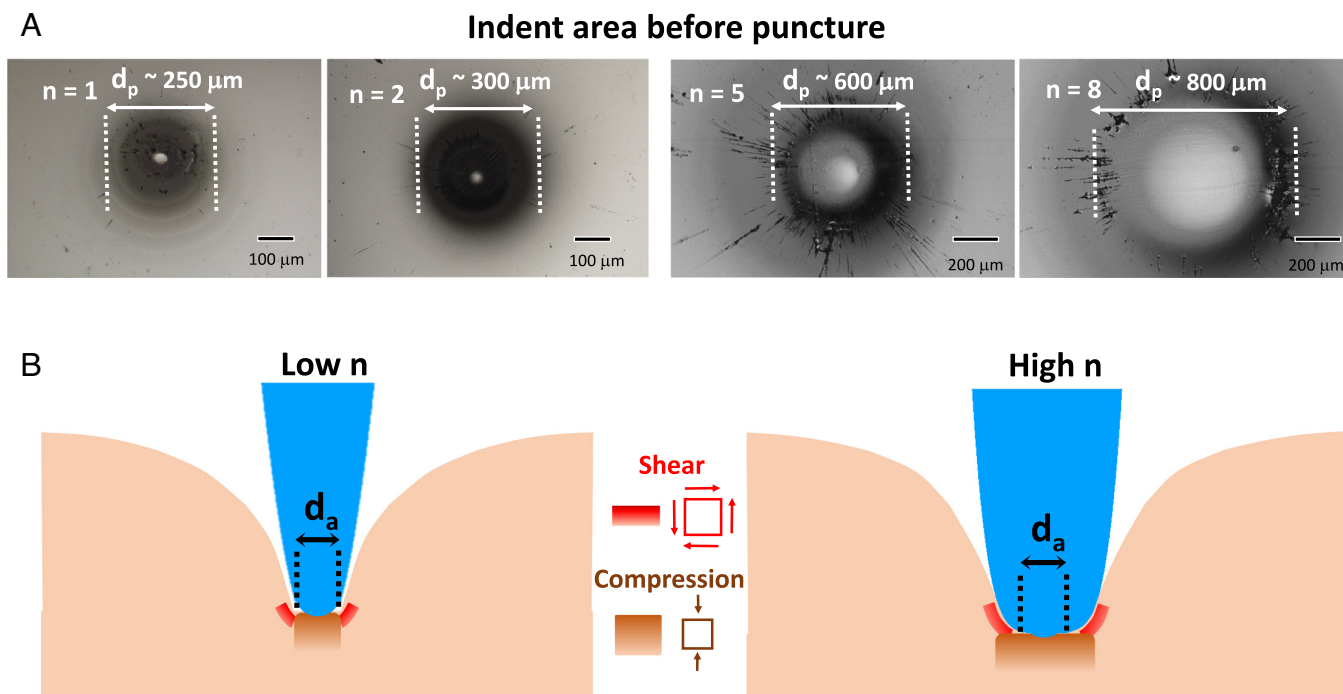
Fig. 5. The impact of taper exponent on penetration. (*A*) Images of indent areas just before puncture (after the stinger is withdrawn). Plastic deformation is identified by the permanent change of contrast; the diameter of the deformation zone is indicated as d_p. (*B*) Schematic illustration of the deformation and stress in the indentation process for different stingers. The puncture is caused by the combination of compression beneath the indenter and shear along the circumference of the contact edge. For stingers with low *n*, both the compression and shear stress are mainly generated by the immediate stinger tip (d_a). For stingers with high *n*, the shear stress is concentrated outside the immediate stinger tip ($>d_a$) and penetration requires compression of a substrate zone (brown region in the *Right* panel) larger than the area beneath the immediate stinger tip (d_a).

for stinger designs. Regarding the penetration mechanisms, more work is warranted, for example, in determining whether cracks under the stinger tip originate from compression directly beneath it or from shearing forces that result in material failure. Nevertheless, when approaching sharp tips, all designs will eventually be limited by an inescapable trade-off: that between delaying elastic buckling and easing penetration.

Conclusion

Our study proposes that many biological stingers have evolved to an optimized non-linear shape; they appear to have a universal profile where the diameter (*d*) varies along the longitudinal axis (*x*) according to a power law $x \sim d^n$. The exponent *n* in Nature is found to cluster between 2 and 3, regardless of the size or material composition of the investigated stingers. By combining modeling and experiments, we rationalize this effective strategy in stingers composed of materials with moderate elastic moduli aiming to penetrate skin-like tissues. Such tapering raises the stinger's buckling resistance above the penetration barrier while keeping the latter at a minimum. This adaptation of biological stingers creates an inconspicuous yet robust lethal weapon against predators or rivals; it may also provide inspiration for improving non-metallic needles for engineering or biomedical purposes.

Methods

Measurement of Stinger Dimensions. The variation of the diameter of stingers is measured from literature sources and by analyzing images acquired using an optical microscope (Eclipse LV100ND, Nikon, Tokyo, Japan) and a scanning electron microscope (EI Quanta 400 ESEM, Thermo Fisher, USA). Measurements for radiolarian, bee, cactus, porcupine, and narwhal are based on images in Fig. 1*A*. Dimensions of the other four stingers are obtained from the following image

sources: Ref. 20 for the mosquito; https://alexhyde.photoshelter.com/image/I0000blwxLjZq_Xs for the stinging nettle; www.wildnatureinstitute.org for the whistling thorn; Ref. 5 for the scorpion. The measurement of Robinia is based on our own image as shown in *SI Appendix*, Fig. S7.

Fabrication of Stingers and Substrate. The stingers used for the buckling and penetration tests are fabricated by a 3D printer Asiga MAX (Asiga, Alexandria, Australia) and the material used for printing is Splint 385 (Dentona, Dortmund, Germany), a commercial Methacrylate-based 3D printing resin with a curing wavelength of 385 nm. For all 3D-printed stingers used in all experiments, a hemisphere of curvature radius 0.25 mm is fabricated on the 0.5 mm diameter narrow end to truncate the tapered column. This feature reduces the influence of tip dimension otherwise arbitrarily induced by the resolution of the 3D printer and has other benefits as described in the text. A compressive load deflection curve of a fabricated slender cylinder of uniform diameter and made from the sample printing material is shown in *SI Appendix*, Fig. S8. The load and deflection are normalized by the cross-sectional area and cylinder length, respectively. The slope before buckling (the first load drop) is determined to be ~1.9 GPa. This value is consistent with the modulus parameter in our modeling and is the same order of magnitude as the modulus for biological materials forming natural stingers, e.g., wood (~7 GPa), bone (~8 GPa), keratin (~2.5 GPa), or chitin (~2 GPa).

The substrate used for the penetration tests is fabricated from the PDMS, (Elastomer kit Sylgard 184, Dow Silicones, Midland, MI, USA) by mixing the two components (parts A and B) in the ratio 10:1. The mixture of PDMS solution is cured at 95 °C for 1 h. The thickness of substrate is at least 3 times the penetration depth in the puncture tests.

Mechanical Testing. The buckling and penetration tests are both performed on a mechanical testing machine Zwick (ZwickRoell GmbH & Co. KG) in uniaxial compression. For each measurement, including both buckling and penetration force, at least 3 tests are performed and the average is taken of the measurement results. The testing is displacement controlled and the compression speed is 10 mm/min. The load is measured with load cells of 200 N and 2 kN. For the buckling tests, the printed tapered columns are placed directly between the metal

platens of the testing machine and both upper and lower platens are covered by 40-grit sandpaper to prevent lateral translation of the ends of columns. For the penetration tests, the thick end of the column is fixed on the upper platen and the PDMS substrate is placed on the lower platen as the penetration target.

The stingers (cactus, quince, barberry, and robinia) used for penetrating pigskin are mounted on a plastic holder using super bond. Fresh pig shoulder complete with skin is purchased from REAL supermarket in Saarbruecken and the penetration tests are performed on the area with relatively flat skin.

Justification of Using the Concept of Effective Length. The experimentally measured critical buckling loads, F_{cr} for the 3D-printed stingers with $L_0 = 40$ mm deviate from the theoretical predictions. This is caused mainly by the experimental setup (*Inset* in Fig. 2C). Sandpaper is placed at the two ends of the columns for impeding their lateral movement, but this also imposes constraints on column end rotation so that true pinned–pinned BCs are not achieved. This feature causes a higher buckling load in the experiments than predicted by pinned–pinned BCs in the theoretical calculations. However, the constraint on column end rotation does not eliminate it completely and some column end rotation does occur during buckling. Therefore, the BCs imposed are neither those of pinned–pinned conditions nor of complete end constraint. In Euler buckling models, an effective length can be introduced to capture the critical buckling load for columns with such intermediate constraints on end rotation. Here, the same concept is adapted to capture the effect of the BCs for the tapered columns that arise in our experiments. The green curve in Fig. 2C shows the theoretical buckling load for tapered columns with length $L_0^{eff} = 30$ mm under pinned–pinned BCs, which fits well with our experimental results. Moreover, we verified that the factor 0.75 is also applicable to experimental results for additional 3D-printed stingers with different design parameters tested in the same experimental setup (results shown in *SI Appendix*, Fig. S3). This further validates our approach of using an effective length that is 0.75 times the actual stinger length to bring the theoretical predictions for the critical buckling load into agreement with the experimental results.

The Fixed and Varied Parameters in Fig. 2 *D–G*. (*D*): The fixed parameters are $AR = 0.10$, $E = 1.9$ GPa and $TBR = 0.125$. The varied parameters are $d_0 = 2$ mm (resulting in $L_0 = 20$ mm and $d_a = 0.25$ mm), $d_0 = 4$ mm (resulting in $L_0 = 40$ mm and $d_a = 0.5$ mm), and $d_0 = 6$ mm (resulting in $L_0 = 60$ mm and $d_a = 0.75$ mm). (*E*) The fixed parameters are $E = 1.9$ GPa, $d_0 = 4$ mm, $d_a = 0.5$ mm, and $TBR = 0.125$. The varied parameters are $AR = 0.06$ (resulting in $L_0 = 66.67$ mm), $AR = 0.10$ (resulting in $L_0 = 40$ mm), and $AR = 0.12$ (resulting in $L_0 = 33.33$ mm). (*F*) The fixed parameters are $AR = 0.10$, $L_0 = 40$ mm, $d_0 = 4$ mm, $d_a = 0.5$ mm, and $TBR = 0.125$. The varied parameters are $E = 1$ GPa, $E = 1.9$ GPa, and $E = 5$ GPa. (*G*) The fixed parameters are $AR = 0.10$, $L_0 = 40$ mm, $d_0 = 4$ mm, and

$E = 1.9$ GPa. The varied parameters are $TBR = 0.01$ (resulting in $d_a = 0.04$ mm), $TBR = 0.05$ (resulting in $d_a = 0.2$ mm), and $TBR = 0.125$ (resulting in $d_a = 0.5$ mm).

Imaging of Indents. The indents before and after puncture in the penetration tests are imaged with an optical microscope (Eclipse LV100ND, Nikon, Tokyo, Japan). The images before puncture are taken by unloading the stingers and removing them from the PDMS substrate.

Finite Element Analyses (FEA). FEA using Abaqus (23) were utilized to discern the stress distribution during the indentation process involving stingers of varying shapes. Both the stinger and the substrate were modeled as axisymmetric. The geometric configuration of the stinger was defined as Eq. **1**. While the stinger was modeled as analytically rigid, the soft substrate incorporated a Neo-Hookean constitutive relationship, characterized by an initial Young's modulus of 1 MPa and a Poisson's ratio of 0.45. Owing to pronounced stress concentrations, a finer mesh was employed for the substrate in proximity to the contact zone. The contact interface was defined to possess hard and frictionless characteristics. For meshing, the stinger utilized RAX2, whereas the substrate employed CAX4R.

Data, Materials, and Software Availability. All study data are included in the article and/or *SI Appendix*.

Author affiliations: ^aDepartment of Materials Science and Engineering, College of Engineering and Applied Sciences, Nanjing University, Nanjing 210023, China; ^bInstitute for New Materials–Leibniz Institute for New Materials, Saarbrücken 66123, Germany; ^cSchool of Science, Harbin Institute of Technology, Shenzhen 518055, China; ^dDepartment of Advanced Manufacturing and Robotics, College of Engineering, Peking University, Beijing 100871, China; ^eDepartment of Nanoengineering, University of California, San Diego, CA 92093; ^fDepartments of Materials and Mechanical Engineering, University of California, Santa Barbara, CA 93106; ^gDepartment of Materials Science and Engineering, Saarland University, Saarbrücken 66123, Germany; and ^hDepartment of Mechanical and Aerospace Engineering, Program in Materials Science and Engineering, University of California, San Diego, CA 92093

1. L. Li, K. Endo, Phylogenetic positions of "pico-sized" radiolarians from middle layer waters of the tropical Pacific. *Prog. Earth Planet. Sci.* **7**, 70 (2020).
2. W. K. Cho *et al.*, Microstructured barbs on the North American porcupine quill enable easy tissue penetration and difficult removal. *Proc. Natl. Acad. Sci. U.S.A.* **109**, 21289–21294 (2012).
3. M. E. Malainine *et al.*, Structure and morphology of cladodes and spines of *Opuntia ficus-indica*. Cellulose extraction and characterisation. *Carbohydr. Polym.* **51**, 77–83 (2003).
4. Z. L. Zhao *et al.*, Structures, properties, and functions of the stings of honey bees and paper wasps: A comparative study. *Biol. Open* **4**, 921–928 (2015).
5. Z. L. Zhao, T. Shu, X. Q. Feng, Study of biomechanical, anatomical, and physiological properties of scorpion stingers for developing biomimetic materials. *Mater. Sci. Eng. C-Mater. Biol. Appl.* **58**, 1112–1121 (2016).
6. J. D. Currey, K. Brear, P. Zioupos, Dependence of mechanical properties on fibre angle in narwhal tusk, a highly oriented biological composite. *J. Biomech.* **27**, 891–897 (1994).
7. T. A. McMahon, J. T. Bonner, J. Bonner, *On Size and Life* (Scientific American Library, 1983).
8. K. H. Jensen, J. Knoblauch, A. H. Christensen, K. S. Haaning, K. Park, Universal elastic mechanism for stinger design. *Nat. Phys.* **16**, 1074 (2020).
9. P. W. Freeman, C. A. Lemen, The trade-off between tooth strength and tooth penetration: Predicting optimal shape of canine teeth. *J. Zool.* **273**, 273–280 (2007).
10. A. R. Evans *et al.*, A universal power law for modelling the growth and form of teeth, claws, horns, thorns, beaks, and shells. *BMC Biol.* **19**, 14 (2021).
11. M. A. Meyers, P. Y. Chen, A. Y. M. Lin, Y. Seki, Biological materials: Structure and mechanical properties. *Prog. Mater. Sci.* **53**, 1–206 (2008).
12. S. A. Ranamukhaarachchi *et al.*, Development and validation of an artificial mechanical skin model for the study of interactions between skin and microneedles. *Macromol. Mater. Eng.* **301**, 306–314 (2016).
13. S. P. Timoshenko, J. M. Gere, *Theory of Elastic Stability* (McGraw-Hill, ed. 2, 1963).
14. P. S. L. Anderson, Making a point: Shared mechanics underlying the diversity of biological puncture. *J. Exp. Biol.* **22**, jeb187294 (2018).
15. B. Zhang, P. S. L. Anderson, Modelling biological puncture: A mathematical framework for determining the energetics and scaling. *J. R. Soc. Interface.* **19**, 20220559 (2022).
16. O. A. Shergold, N. A. Fleck, Mechanisms of deep penetration of soft solids, with application to the injection and wounding of skin. *Proc. R. Soc. A-Math. Phys. Eng. Sci.* **460**, 3037–3058 (2004).
17. A. Stevenson, K. Abmalek, On the puncture mechanics of rubber. *Rubber Chem. Technol.* **67**, 743–760 (1994).
18. S. Fakhouri, S. B. Hutchens, A. J. Crosby, Puncture mechanics of soft solids. *Soft Matter.* **11**, 4723–4730 (2015).
19. C. W. Barney, C. Chen, A. J. Crosby, Deep indentation and puncture of a rigid cylinder inserted into a soft solid. *Soft Matter.* **17**, 5574–5580 (2021).
20. X. Kong, C. W. Wu, Mosquito proboscis: An elegant biomicroelectromechanical system. *Phys. Rev. E Stat. Nonlin. Soft Matter Phys.* **82**, 011910 (2010).
21. B. Bar-On, On the form and bio-mechanics of venom-injection elements. *Acta Biomater.* **85**, 263–271 (2019).
22. H. M. van Tol, A. J. Irwin, Z. V. Finkel, Macroevolutionary trends in silicoflagellate skeletal morphology: The costs and benefits of silicification. *Paleobiology* **38**, 391–402 (2012).
23. ABAQUS 6.14 Documentation, Dassault systems (Simulia Corporation, Providence, RI, 2014).